PAPER

Check for updates

Scalable single-step deposition of recyclable TiO₂@Au monolayer coatings for enhanced visible-light photocatalysis of methylene blue dye†

Shaobo Zhang,[b] Jun Yang,[c] Ranhong Wu,[c] Die Li,[ab] Xinjiang Zhang,[c] Mingshan Zheng,[c] Yi Jiang,[c] Haiguang Ma, [ID] ⋆[ab] Deren Yang [ID] [ab] and Xuegong Yu [ID] ⋆[ab]

Titanium dioxide@gold (TiO₂@Au) nanocomposite monolayers with enhanced visible-light photocatalysis were synthesized *via* an air–water interfacial self-assembly and pyrolysis strategy. This method simultaneously embeds Au nanoparticles (5–20 nm) within TiO₂ and reduces the bandgap from 3.02 eV to 2.66 eV *via* interfacial charge redistribution. In a 200 ml aqueous reaction system, the TiO₂@Au monolayers demonstrated a visible-light-driven methylene blue degradation rate of 0.0054 min^{-1}-3.6-fold higher than pure TiO₂, attributed to Au's localized surface plasmon resonance (LSPR) enhancing visible-light absorption and interfacial electron transfer. The system maintained 99.2% activity retention over five cycles, showcasing unprecedented stability in large-volume wastewater treatment scenarios. This method leverages self-limiting assembly at the air–water interface to orchestrate the molecular packing of organometallic precursor films, which upon pyrolysis yield centimeter-scale nanocomposite monolayers. The developed methodology provides a practical pathway for industrial photocatalytic wastewater purification.

1. Introduction

Water pollution poses escalating threats to human health and ecosystems globally.[1,2] Contaminated water sources are responsible for waterborne diseases that claim over 2.2 million lives annually.[3] Among the various pollutants, organic contaminants such as dyes are particularly hazardous due to their toxicity and detrimental effects on both human health and the environment.[4] In recent years, photocatalysis has emerged as a promising solution for wastewater treatment, owing to its cost-effectiveness, operational simplicity, and environmental sustainability.[5–9] However, conventional photocatalysts like titanium dioxide (TiO₂) and zinc oxide (ZnO) exhibit limited photocatalytic activity under visible light due to their wide bandgaps (*e.g.* 3.2 eV for anatase TiO₂) and rapid recombination of photogenerated charge carriers.[10–12] To address these limitations, the formation of heterojunctions between metal nanoparticles (NPs) and semiconductor photocatalysts has been

explored. This approach leverages the local surface plasmon resonance (LSPR) effect of metal NPs, which enhances light absorption, charge separation, and surface reactivity.[10,13–15] For instance, TiO₂@gold (TiO₂@Au) nanocomposites have demonstrated exceptional potential in water treatment applications due to their superior photocatalytic and adsorption properties.[11,13,16–18] Notably, Lee *et al.* immobilized TiO₂–Au nanoplasma photocatalysts onto a sponge, significantly improving the photocatalytic efficiency by enhancing the contact between rhodamine B and the photocatalyst.[19] Despite these advancements, challenges such as high costs, limited reusability, and scalability hinder the practical application of TiO₂@Au nanocomposites in industrial settings.

The synthesis of TiO₂@Au nanocomposites has been extensively studied, with various chemical and physical methods being employed, including chemical reduction,[20] photo-deposition,[21] deposition–precipitation[22,23] and physical vapor deposition.[24,25] However, these methods often involve complex, multi-step processes that are time-consuming, costly, and impractical for large-scale industrial applications.[26] Additionally, the immobilization of photocatalysts into polymers or other matrices to enhance recyclability often compromises their photocatalytic performance. In contrast, solid-state thermal decomposition offers a cost-effective, solvent-free, and straightforward approach for synthesizing nanoparticles.[27] This method has been successfully applied to produce various nanoparticles, including Au, copper oxide, and nickel oxide,[27–31]

[a]State Key Laboratory of Silicon and Advanced Semiconductor Materials, School of Materials Science and Engineering, Zhejiang University, Hangzhou, Zhejiang 310027, China

[b]ZJU-Hangzhou Global Scientific and Technological Innovation Center, Zhejiang University, Hangzhou 311200, China

[c]Institute of Quartz, Ferrotec (Zhejiang) Quartz Technology Co., Ltd, Quzhou 324000, China. E-mail: mahaiguang@zju.edu.cn; yuxuegong@zju.edu.cn

Paper

as well as nanocomposites.[32,33] However, the aggregation of nanoparticles during synthesis often limits their performance and application.

In this study, we introduce an innovative one-step method for synthesizing TiO$_2$@Au nanocomposite monolayers, leveraging self-limiting assembly at the air–water interface to precisely control the molecular packing of organometallic precursor films. This monolayer, characterized by a reduced bandgap of 2.66 eV, is firmly anchored to the substrate through the thermal decomposition of the precursor film. This novel approach not only ensures robust attachment to the substrate but also significantly enhances the reusability of the nanocomposites in sewage treatment applications. The precursor film is prepared *via* a rapid self-assembly process of organometallic molecules at the air–water interface, enabling efficient and scalable fabrication. By incorporating gold nanoparticles with diameters ranging from 5 to 20 nm alongside TiO$_2$ nanoparticles, the photocatalytic activity of the resulting TiO$_2$@Au nanocomposites is substantially enhanced. Experimental results demonstrate that the degradation rate of methylene blue (MB) dye by the synthesized TiO$_2$@Au nanocomposites is 1.5 times and 3.6 times higher than that of pure TiO$_2$ nanoparticle films under ultraviolet and visible light, respectively. Specifically, degradation rates of 0.0095 min^{-1} and 0.0054 min^{-1} were achieved using a 2.5 cm × 2.5 cm sample in a 200 ml MB solution. These findings highlight the exceptional performance and practical viability of the developed photocatalysts, offering new opportunities for their application in diverse environmental remediation fields. The simplicity, scalability, and efficiency of this method make it a promising candidate for addressing water pollution challenges on a larger scale.

2. Experimental

2.1 Materials

Gold resinate was obtained from Grimat Engineering Institute Co., Ltd (China). Titanium acetylacetonate, xylene and methylene blue (MB) were obtained from Macklin Biochemical Co., Ltd (China). The 400-mesh 304 stainless steel was procured from Ruikai Metal Products Co., Ltd. Ethanol and acetone were obtained from Sinopharm Chemical Reagent Co., Ltd (China). All chemicals were analytically pure. Deionized water derived from laboratory-made. Commercial glass slides were used as substrates.

2.2 Preparation of TiO$_2$@Au films

A mixture of gold resinate and titanium acetylacetonate was prepared by dissolving them in xylene and stirring for 30 min. The concentration of gold resinate was 15, 60 and 120 mg ml^{-1}, and that of titanium acetylacetonate was 200 mg ml^{-1}. The two solutions were then mixed in a 1 : 1 ratio and stirred for an additional 2 h. The mixed solution was either added directly onto the water surface or pre-dispersed on a glass slide, and then spread on the air–water interface to create a precursor film through a self-assembly process. The formed film was transferred on the substrate and dried at 60 °C to remove water, and

the process was repeated to achieve films of different thicknesses. Finally, the glass slides coated with precursor film were placed in a tube furnace and subjected to rapid annealing at 600 °C for 1 hour under an air atmosphere. In the following sections, samples coated with Au nanoparticle films are denoted as AuNPs, those coated with TiO$_2$ films are labelled as TiO$_2$, samples with a single layer of TiO$_2$@Au films are referred to as TiO$_2$@Au, and samples with three layers of TiO$_2$@Au films are designated as TiO$_2$@Au-3.

2.3 Materials characterization

The morphology of the prepared nanoparticles was characterized using atomic force microscopy (AFM, Bruker Dimension Icon, Germany) and transmission electron microscopy (TEM, FEI Talos F200X G2, USA) at 200 kV. The elemental distribution of TiO$_2$@Au was characterized by energy dispersive spectroscopy (EDS). Microscopic morphology of steel wire mesh was observed by scanning electron microscopy (SEM, ZEISS GeminiSEM 300, Germany). The crystal structure of films was verified by grazing incidence X-ray diffraction (GIXRD, Rigaku Smartlab 9 kW, Japan) with Cu Kα radiation in the range of 20°–80°, while the nanoparticle size of Au was calculated by the Scherrer formula. The elemental compositions of films were measured by X-ray photoelectron spectroscopy (XPS, Thermo Scientific K-Alpha, USA) with Al Kα X-ray source and analysed by Advantage software. The absorption spectra at 300–800 nm were measured by UV-vis diffuse reflectance spectrometer (DRS, Shimadzu UV-3600i Plus, Japan). The concentration of MB was measured by UV-vis spectrophotometer (China).

2.4 Characterization of photocatalytic activity

The MB was selected as the organic compound for photocatalytic degradation experiments. A 2.5 cm × 2.5 cm glass sample coated with a TiO$_2$@Au monolayer was placed in a beaker containing 200 ml of a MB solution with a concentration of 10 mg l^{-1}. The solution was continuously stirred in the dark for about 60 minutes to reach an adsorption–desorption equilibrium between the photocatalyst and the dye. After that, a 20 W UV lamp and a 300 W xenon lamp were positioned above the beaker to initiate photocatalytic degradation, respectively. The distance between the light source and the water surface in the beaker was set at 25 cm, as shown in Fig. S1.† During the irradiation, the solution was kept stirred. Every 15 minutes, 5 ml of the solution was taken and was measured with a UV-visible spectrophotometer.

3. Results and discussion

3.1 Microstructure and physical properties

In the Au and TiO$_2$ nanoparticles and their composites were prepared *via* the solid-state thermal decomposition method. The crucial step involves assembling the organometallic molecules into a solid thin film at the air–water interface (Fig. 1a). Specifically, at room temperature, the precursor solution is directly spread onto the water surface using a pipette or an injector. The precursor molecules readily assemble into a film
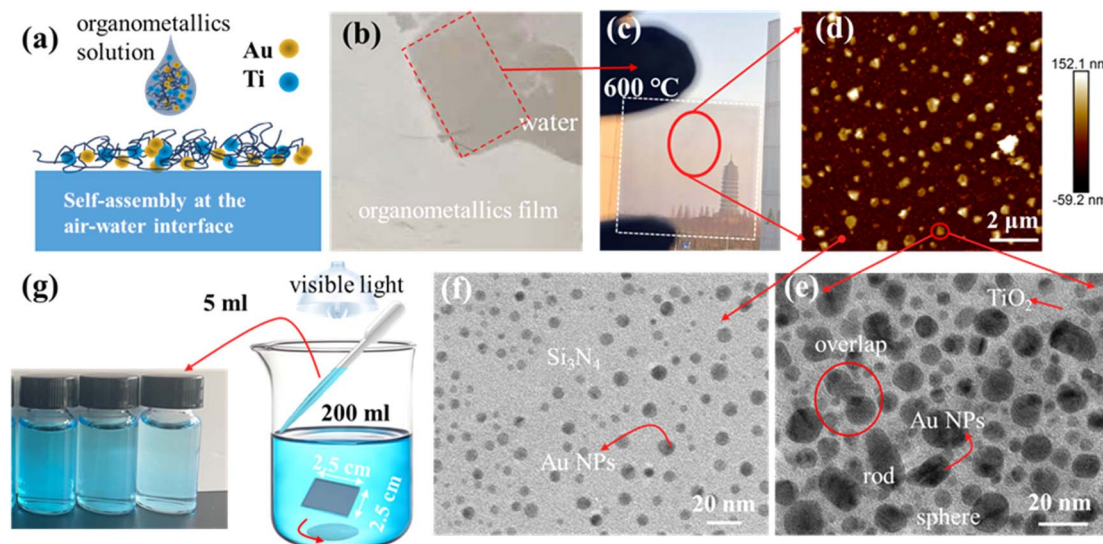
Fig. 1 The fabrication process of TiO₂@Au nanocomposite and its application in sewage treatment. (a) and (b) The process of preparing the precursor film at the air−water interface and the photograph of the film floating on the water surface. (c) The photograph of TiO₂@Au nanocomposite film deposited on glass. (d)–(f) AFM and TEM image of the TiO₂@Au nanocomposite film. (g) Application of the TiO₂@Au nanocomposite in the treatment of organic pollutants under visible light.

on the water subphase (Fig. 1b), facilitating the efficient formation of the precursor film. Subsequently, the films are transferred onto substrates such as glass slides. The samples are then dried at 60 °C and placed in a tube furnace, where they are annealed in air at temperatures ranging from 300 to 600 °C to form the nanoparticles. Fig. 1c displays a photograph of the TiO₂@Au nanocomposite film on a glass substrate. The microstructure of the film was analysed using AFM (Fig. 1d). Additionally, a TEM image confirms the transformation of the initial precursor thin film into nanoparticles (Fig. 1e). These results demonstrate that the precursor thin film formed monodisperse nanoparticles, and the surface of the titanium dioxide nanoparticles was uniformly distributed with gold nanoparticles (AuNPs) (Fig. 1e). The morphology of the AuNPs includes both spherical and rod-like structures, whereas those deposited on the silicon carbide support membrane are exclusively spherical, as depicted in Fig. 1f. Furthermore, the overlapping gold particles on the TiO₂ nanoparticles suggest the presence of gold nanoparticles within the TiO₂ particles. This structural configuration could prevent the detachment of gold nanoparticles and thus contributes to improving the stability of the composite material. Fig. 1g illustrates the experimental setup for measuring the degradation rate of methylene blue (MB) in solution using the synthesized photocatalysts.

In Fig. 2a and b, the TEM images show the AuNPs prepared by the decomposition of the gold resinate film. The AuNPs are distributed homogeneously, with a spherical morphology. The size histograms of the TEM images reveal that the size ranges from 4–12 nm as shown in (Fig. S2†). Gold resinate is a traditional material for preparing liquid bright gold. It starts to decompose at approximately 116 °C (Fig. S3†). When the calcination temperature reaches 350 °C, the gold resinate film can be converted into Au NPs (Fig. S4†). This can be used to prepare

Au NPs on stainless steel mesh (Fig. S5†). It has been found that the size of the AuNPs is not positively correlated with the thickness of the precursor film. Neither increasing the density of the precursor solution nor adding the number of precursor films leads to a significant increase in the size of the Au NPs, but the number density increases markedly compared to samples fabricated using three precursor layers (Fig. S6†). The absorption spectra of AuNPs created at various temperatures exhibit the characteristic LSPR peak near 540 nm (Fig. 2c). As the temperature was raised from 350 to 600 °C, the LSPR FWHM of the Au NPs narrowed, which indicated more uniformity of the nanoparticles. In addition, the TiO₂ nanoparticles prepared at 600 °C exhibit a plane spacing of 0.351 nm, which is equivalent to the (101) plane of anatase (Fig. 2d and e). The size of these nanoparticles varies widely. The distribution ranges from 100 to 280 nm, and the mean size is 194.0 nm (Fig. S7†). A photograph of the TiO₂@Au nanocomposite film is shown in Fig. 2f. There are two peaks in the absorption spectra of TiO₂@Au and TiO₂@Au-3. The peak at around 370 nm is caused by TiO₂, and the one at 520 nm comes from the localized surface plasmon resonance (LSPR) effect of AuNPs. This indicates that the film synthesized from the mixed precursors consists of TiO₂ and AuNPs. Compared to pure gold nanoparticles, the localized surface plasmon resonance (LSPR) absorption peak of TiO₂@Au composite nanostructures exhibits a broader full width at half maximum (FWHM). This is because the individually synthesized gold nanoparticles have a relatively uniform morphology (as shown in Fig. 2a), whereas during the formation of the composite nanostructure, the morphology of the gold nanoparticles undergoes significant changes, resulting in irregular shapes such as nanorods. This morphological variation leads to broadening of the plasmonic resonance peak, which can enhance the absorption range of visible light and thereby
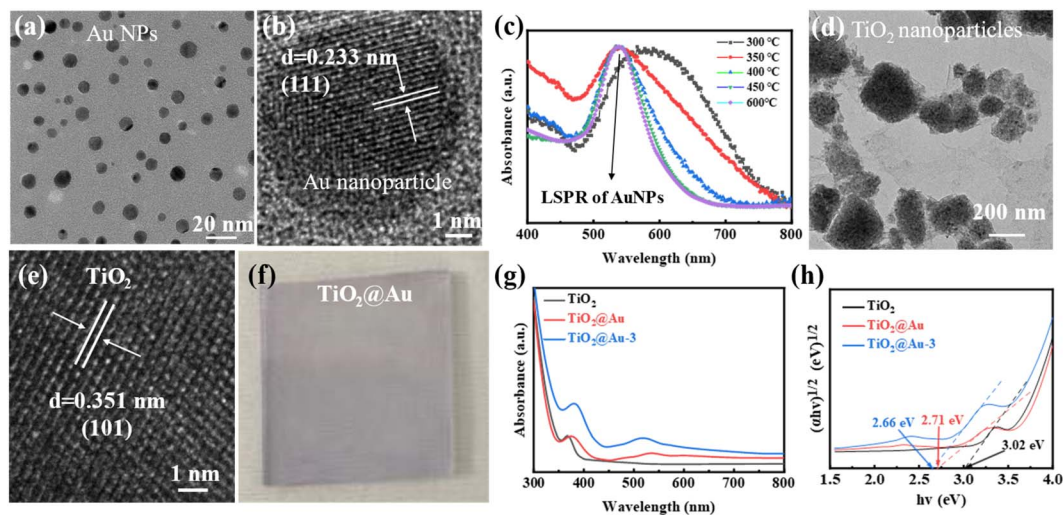
Fig. 2 (a) and (b) TEM images depicting the morphology of AuNPs. (c) The absorptance spectra of gold nanoparticles prepared at different temperature, revealing the LSPR effect. (d) and (e) TEM images presenting the structural features of TiO_2. (f) The photograph of TiO_2@Au film deposited on glass. (g) and (h) Absorptance spectra of TiO_2, TiO_2@Au and TiO_2@Au-3, along with their corresponding bandgap values.

improve catalytic efficiency. Furthermore, the bandgap of the nanocomposite film can be tuned by the AuNPs, as shown in Fig. 2h. Moreover, the atomic force characterization of the structures obtained after annealing different precursor films is as shown in the Fig. S8.† The surfaces are all composed of separated nanoparticles, and the composite film structure can be achieved by sequentially transferring titanium and gold precursor molecular films, with the nanoparticles being more densely packed, as illustrated in the Fig. S9.†

In addition, the optical bandgap was calculated by using the Tauc plot method.[34] The TiO_2 nanoparticles film has a typical bandgap energy of 3.02 eV, falling within the usual range of TiO_2 (3.0–3.2 eV).[35,36] After decorating with Au nanoparticles, the bandgap of the TiO_2@Au nanocomposite is reduced to 2.71 eV, while that of the TiO_2@Au-3 nanocomposite is further

decreased to 2.66 eV. This is ascribed to the plasmonic properties[37] and oxygen vacancies,[38–41] which can enhance the light absorption and promote the generation of charge carriers through plasmon-induced resonance energy transfer. The reduced band gap of the TiO_2@Au nanocomposite makes it more efficient for applications in photocatalysis.

TEM images reveal that the AuNPs are uniformly distributed on the TiO_2 nanoparticles, with the Au NPs retaining their spherical shape, consistent with that of individual AuNPs (Fig. 3a and b). To elucidate the detailed atomic structure of the TiO_2@Au nanocomposite, high-resolution TEM (HRTEM) was employed. The lattice spacings of 0.21 nm and 0.33 nm correspond to the (111) crystal plane of cubic Au and the (101) crystal plane of anatase TiO_2, respectively, as illustrated in Fig. 3c. To further investigate the dispersion of the supported Au particles
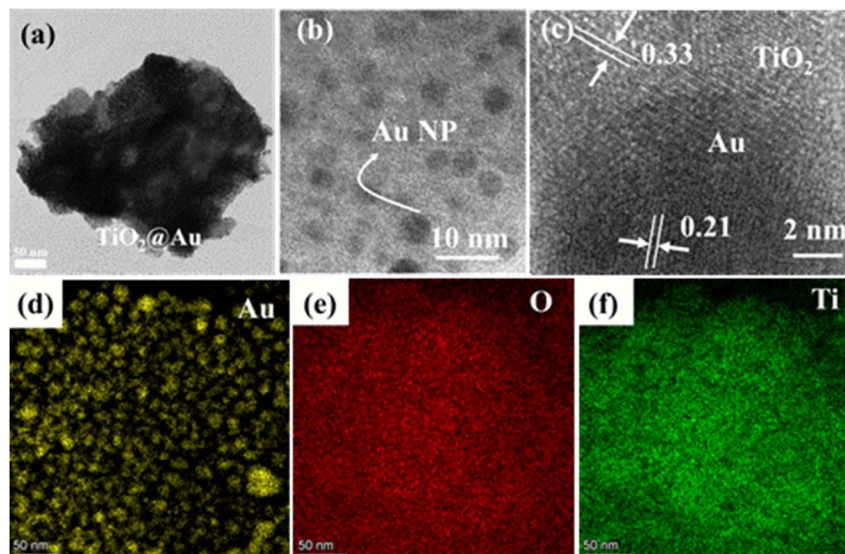

Fig. 3 (a) and (b) TEM images of TiO_2@Au. (c) HR-TEM image of TiO_2@Au. (d)–(f) EDS mapping images.

on the TiO_2 surface, the nanocomposites were analyzed using energy-dispersive X-ray spectroscopy (EDS) mapping in scanning transmission electron microscopy (STEM) mode. The EDS mapping images of TiO_2@Au confirm the uniform distribution of Au (yellow), O (red), and Ti (green) elements, as depicted in Fig. 3d–f.

3.2   Chemical structure

Grazing-incidence X-ray diffraction (GIXRD) analysis was conducted on the monolayer TiO_2@Au composite. Fig. 4a displays the GIXRD patterns of TiO_2@Au monolayer after calcining at 600 °C. Due to the significant size difference between Au NPs and TiO_2, it is necessary to control a suitable grazing incidence angle to characterize both TiO_2 and Au simultaneously, which is set to 0.2° here. The diffraction peaks of Au film at 38.4° (111), 44.4° (200), 65.0° (220), and 78.1° (311) correspond to JCPDS#04-0784, indicating the formation of Au NPs. The TiO_2 film only has an obvious diffraction peak at $2\theta = 25.2°$, which is typical of anatase TiO_2. The crystal structure of TiO_2 shows no change after incorporating with Au NPs (Fig. 4a).

The elemental composition and characteristic electronic states of the prepared films were characterized using XPS. The presence of Ti and Au signals in the spectra of TiO_2@Au film indicates effective deposition of TiO_2 and Au NPs on the substrate (Fig. 4b). Increasing the number of precursor layers leads to significantly enhanced absorption peak intensities for Ti and Au, indicating an increased content of TiO_2 and AuNPs. The elemental contents analysed by Advantage software (Table 1). The detected carbon content (33.22 at%) with a characteristic XPS peak at 284.7 eV may originate from organic precursors or surface contamination, and while carbon materials are known to enhance photocatalytic performance, the exact origin and role of carbon in our system warrant further investigation.[42–44] Compared to the TiO_2@Au, the Ti and Au elements of TiO_2@Au-3 grow to about 3 times. Additionally, the Ti and Au elements on

Table 1   The chemical element composition measured by XPS

Samples	Content (at%)			
	C	O	Ti	Au
TiO_2	33.22	65.09	1.69	—
TiO_2@Au	32.08	65.44	1.78	0.70
TiO_2@Au-3	26.63	66.09	5.22	2.06

the TiO_2@Au film were fitted and analysed. The characteristic peaks at 458.4 eV and 464.1 eV correspond to Ti $2p_{3/2}$ and Ti $2p_{1/2}$, respectively (Fig. 4c).[45] The binding energy of 83.2 and 86.8 eV for Au $4f_{7/2}$ and Au $4f_{5/2}$ matching that of metallic Au (Fig. 4d).[24,46] The Ti 2p XPS spectra in Fig. 4c reveal distinct binding energies of 458.4 eV and 464.1 eV for Ti $2p_{3/2}$ and Ti $2p_{1/2}$, respectively, for the TiO_2@Au nanocomposite monolayer. In comparison, the Ti 2p spectrum of the pure TiO_2 nanoparticle film shows binding energies of 458.9 eV and 464.6 eV for Ti $2p_{3/2}$ and Ti $2p_{1/2}$. The introduction of Au nanoparticles induces a significant negative shift in the binding energies relative to pure TiO_2. From Fig. 4d, the binding energies of Au $4f_{7/2}$ and Au $4f_{5/2}$ are attributed to metallic gold (Au0). This confirms that calcination at 600 °C in air does not lead to the formation of gold oxide.[24,47] However, compared to the binding energy of 84.0 eV for bulk Au $4f_{7/2}$,[43] a significant negative shift of 0.8 eV is observed for the TiO_2@Au films. The shift in the binding energy of Ti 2p and Au $4f_{7/2}$ suggests a strong interaction between the Au nanoparticles and the TiO_2 matrix.[48,49]

3.3   Photocatalytic performance

As depicted in Fig. 5a and b, when a semiconductor such as TiO_2 is exposed to light with energy equal to or greater than its bandgap energy, it efficiently generates electron–hole (e^-/h^+) pairs. In this process, the holes remain in the valence band, while the electrons are excited into the conduction band. Due to the difference in work functions between Au ($\sim$5.2 eV) and TiO_2 ($\sim$4.8 eV), a Schottky barrier forms at the interface between the metal and the semiconductor.[50] This Schottky barrier facilitates the transfer of electrons from the conduction band of TiO_2 to the surface of Au nanoparticles under UV light irradiation. The electrons transferred to the Au nanoparticles can then react with adsorbed oxygen (O_2) to form highly reactive superoxide radicals ($^{\bullet}O_2^-$). Simultaneously, the dispersed Au nanoparticles act as electron sinks, further promoting the reduction of O_2 on their surfaces to generate $^{\bullet}O_2^-$. Meanwhile, the holes in the valence band of TiO_2 migrate to the semiconductor surface, where they react with adsorbed water (H_2O) and hydroxyl ions (OH^-) to produce hydroxyl radicals ($^{\bullet}OH$). These reactive species, namely $^{\bullet}O_2^-$ and $^{\bullet}OH$, play a crucial role in the degradation of target pollutants by oxidizing them during the photocatalytic process.

The TiO_2@Au nanocomposite enhances visible-light photocatalysis through two synergistic mechanisms:[8,9,51] (1) plasmonic Au nanoparticles extend light absorption via LSPR-induced hot electron injection into the conduction band of TiO_2, and (2) the generated charge carriers (e^-/h^+) react with
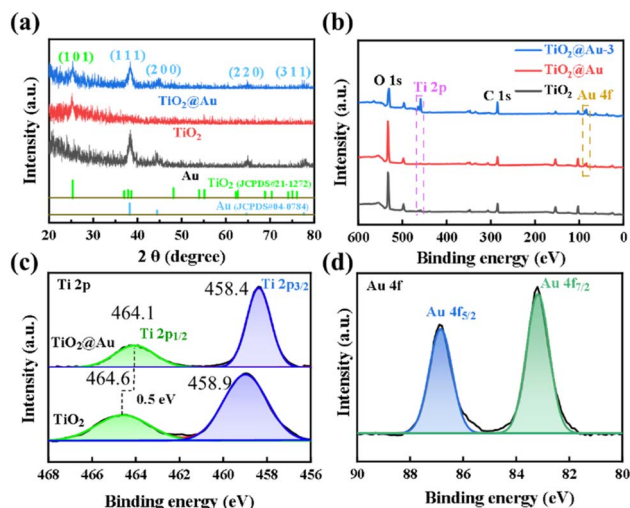

Fig. 4 (a) The GIXRD patterns of films. (b) The XPS spectra. (c) Fitted spectra of Ti 2p on the TiO_2 and TiO_2@Au film surfaces. (d) Fitted spectra of Au 4f on the TiO_2@Au film surfaces.
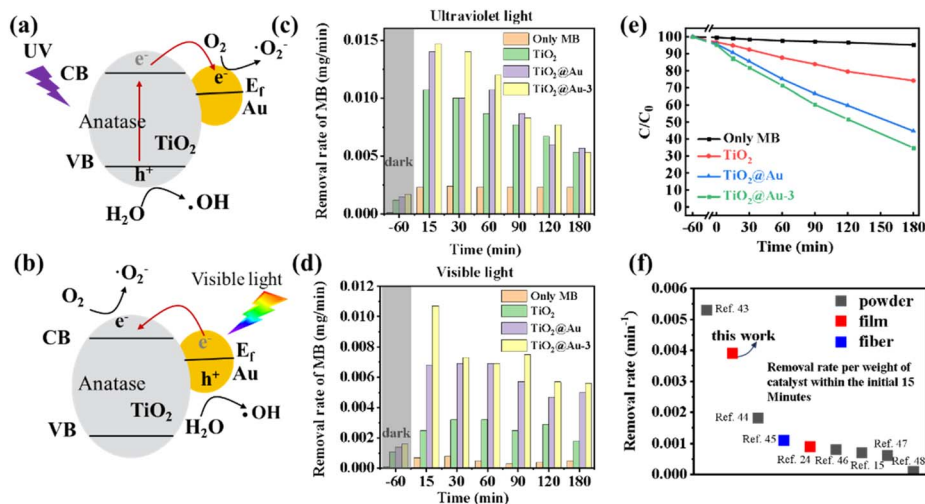
Fig. 5 (a) and (b) Schematic illustration of an electron transfer mechanism for photodegradation of MB dye using the TiO_2@Au nanocomposite under UV and visible light, respectively. (c) and (d) The mean removal rate of MB in each time interval under ultraviolet and visible light irradiation for TiO_2, TiO_2@Au, and TiO_2@Au-3 films. (e) The temporal evolution of the concentration of the MB organic compound in an aqueous solution under visible light for various photocatalysts of TiO_2, TiO_2@Au and TiO_2@Au-3. (f) Removal rate per weight of catalyst within the initial 15 minutes of different catalysts with various morphology.

Table 2 Performance comparison of TiO_2@Au with reported photocatalysts for MB degradation

Photocatalyst	Morphology	Bandgap (eV)	Xenon lamp power (W)	Catalyst (mg)	Density (mg l^{-1})	Volume (ml)	Removal rate (mg min^{-1})	Ref.
TiO_2@Au	Powder	1.12	—	10	32	50	0.053	52
TiO_2@Au	Film	2.66	300	4.1	10	200	0.016	This work
TiO_2@Au	Film	—	300	—	5	50	0.0009	24
Au–WO_3@TiO_2	Powder	—	300	20	30	100	0.036	53
TiO_2@Au	Fiber	2.9	300	4.4	10	40	0.005	54
TiO_2@Au	Powder	2.65	500	50	10	60	0.038	55
TiO_2@Au core–shell	Powder	1.54	300	10	10	20	0.007	15
TiO_2@Au/rGO	Powder	3.43	400	7	9.6	30	0.004	56
TiO_2@Au	Powder	3.05	—	100	10	100	0.013	57

adsorbed species to produce reactive oxygen radicals ($^{\bullet}$OH and $^{\bullet}$O$_2^-$) that mineralize organic pollutants to CO_2 and H_2O, demonstrating superior degradation efficiency compared to pure TiO_2, as shown in Fig. 5b.

The bandgap of the composite nanomaterials decreases as the number of transferred layers increases, as shown in Fig. 2h. Under the UV light irradiation, a lower bandgap corresponds to better catalytic performance of the composite material, as shown in Fig. 5c. However, compared to pure TiO_2, the improvement in photocatalytic performance is limited. The MB removal rates in the solution are 0.0107, 0.014, and 0.0147 mg min^{-1} for TiO_2, TiO_2@Au, and TiO_2@Au-3, respectively. The bar chart in the Fig. 5c illustrates the average degradation rate of MB molecules over time intervals under the action of different catalysts. Higher MB concentrations result in faster degradation rates, indicating that at lower concentrations, the smaller concentration gradient of MB molecules hinders their diffusion to the catalyst surface. As shown in Fig. 5d, under
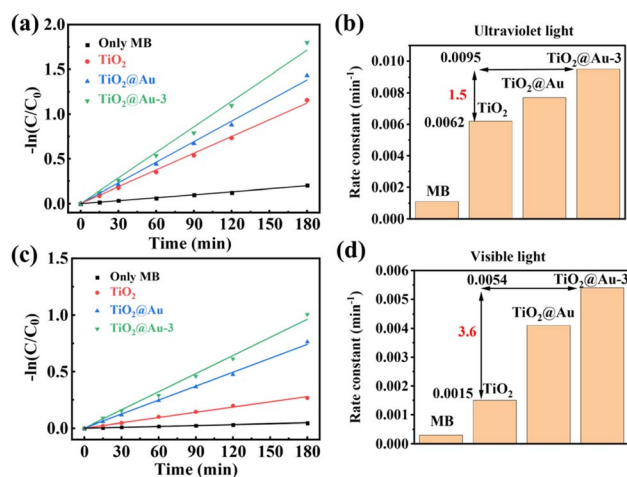

Fig. 6 (a) and (b) The kinetic rate plot of the corresponding photocatalysts under UV and visible light. (c) and (d) Rate constants of MB decomposition for different photocatalysts.
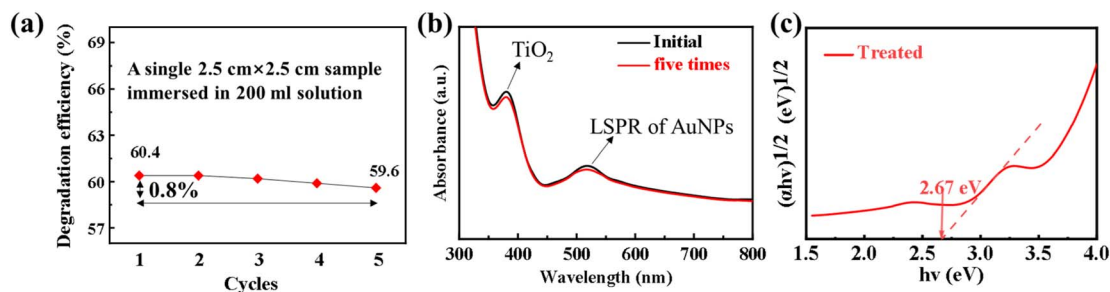
Fig. 7 (a) Reusability of TiO$_2$@Au-3 thin film photocatalyst under visible light. (b) Absorptance spectra of the TiO$_2$@Au-3 thin film calcined at 600 °C: initial state and after five cycles. (c) The bandgap of TiO$_2$@Au-3 thin film after being used five times.

white light irradiation, the catalytic performance of TiO$_2$@Au is significantly enhanced compared to that of pure TiO$_2$, with an improvement of approximately four times. The MB removal rates are 0.0025, 0.0068, and 0.0107 mg min^{-1} for TiO$_2$, TiO$_2$@Au, and TiO$_2$@Au-3, respectively. This demonstrates the substantial role of Au nanoparticles in boosting the photocatalytic activity of the composite under visible light conditions. Similarly, as the MB concentration decreases, the catalytic efficiency also declines. Fig. 5e shows the change in MB concentration over time, where the concentration decreases more rapidly in the initial stage compared to later stages.

To compare the catalytic performances of various catalysts reported in the literature, the catalytic rate per unit mass of each catalyst within the initial 15 minutes was extracted, as shown in Fig. 5f. Powder catalysts dispersed in solution exhibit better catalytic performance, but the performance varies considerably depending on the preparation method. In the initial stage, the higher concentration gradient between the catalyst surface and the solution promotes the diffusion of MB molecules, thereby minimizing the influence of diffusion on the catalytic performance. By comparing the performance of different catalysts at the initial stage, it is concluded that the prepared TiO$_2$@Au-3 demonstrates excellent photocatalytic performance under visible light irradiation. The comparison of photocatalytic degradation of MB dye with other reported photocatalysts as shown in Table 2.

The natural logarithm of the dye concentration plotted against the reaction time yields a straight line, the slope of which represents the pseudo-first-order reaction rate constant, as shown in Fig. 6a and b. Under ultraviolet light, TiO$_2$@Au-3 exhibits the highest catalytic activity, followed by TiO$_2$@Au and TiO$_2$, with the same trend observed under white light. The kinetic rate diagram under white light irradiation shows that the catalytic activity of TiO$_2$@Au-3 and TiO$_2$@Au is significantly enhanced due to the LSPR effect of gold nanoparticles. The bar chart displays the reaction rate constants for different catalytic metals, where under ultraviolet light irradiation, the catalytic rate of TiO$_2$@Au-3 is 1.5 times that of TiO$_2$, and under white light irradiation, it is 3.6 times that of TiO$_2$, as shown in Fig. 6c and d. This indicates that the presence of nanoparticles effectively enhances the performance of the catalyst.

The TiO$_2$@Au-3 film was selected for multiple repeated experiments, each consisting of 60 minutes of adsorption

treatment followed by 180 minutes of visible light irradiation. During the initial dark adsorption phase, the concentration of methylene blue (MB) decreased by 5.2%. However, in subsequent experiments, no significant adsorption was observed (Fig. S10†). The total MB degradation efficiency after the fifth cycle was 59.6%, showing only a slight decrease of 0.8% compared to the initial efficiency of 60.4%. This indicates that the degradation efficiency remained highly consistent throughout the experiments, as illustrated in Fig. 7a.

After five cycles of photodegradation testing, the characteristic absorption peaks of the TiO$_2$@Au-3 film calcined at 600 °C—corresponding to both TiO$_2$ and Au nanoparticles—showed no significant reduction in intensity, indicating that the majority of the nanoparticles remained on the substrate (Fig. 7b). Furthermore, the bandgap of the TiO$_2$@Au-3 film was calculated after treatment and exhibited no notable change, confirming the structural stability of the film, as shown in Fig. 7c. This stability suggests that the composite material retains its electronic and structural integrity under the applied conditions. The consistent band gap further underscores the durability and reliability of the TiO$_2$@Au-3 film over extended use. A slight reduction in the intensity of the characteristic peak was observed, indicating minimal catalyst loss after five cycles. This demonstrates the excellent stability and recyclability of the catalyst, as the majority of its active components remained intact even after repeated use. Such properties are highly advantageous in catalytic applications, as they reduce the need for frequent catalyst replacement and lower operational costs. In summary, these experiments highlight the exceptional degradation activity and stability of the TiO$_2$@Au-3 film, offering a promising approach for the development of recyclable photocatalytic materials.

4. Conclusion

In this study, TiO$_2$@Au nanocomposite monolayers were successfully synthesized through a novel air–water interfacial self-assembly and pyrolysis strategy. This approach simultaneously achieved the embedding of Au nanoparticles (5–20 nm) into the TiO$_2$ matrix and a significant bandgap reduction to 2.66 eV (from 3.02 eV for pristine TiO$_2$). The resulting nanocomposites exhibited a 3.6-fold enhancement in the visible-light-driven degradation rate of methylene blue

$(0.0054 \text{ min}^{-1})$ compared to pure TiO_2, attributed to the LSPR of Au nanoparticles, which improved visible-light absorption and interfacial electron transfer. Notably, the system demonstrated exceptional stability, retaining 99.2% activity over five cycles, highlighting its potential for large-volume wastewater treatment applications. The self-limiting assembly at the air–water interface enabled precise control over molecular packing, yielding centimetres-scale nanocomposite monolayers upon pyrolysis. This scalable approach provides an industrially viable solution for photocatalytic wastewater treatment, demonstrating both efficiency and sustainability for environmental remediation.

Data availability

The data that support the findings of this study are available from the corresponding author upon reasonable request.

Author contributions

Shaobo Zhang: methodology, investigation, data curation, writing – original draft, writing – review & editing. Jun Yang: investigation, methodology. Ranhong Wu: investigation. Die Li: investigation, validation, writing – original draft. Xinjiang Zhang: investigation. Mingshan Zheng: investigation. Yi Jiang: investigation. Haiguang Ma: methodology, data curation, supervision, validation, writing-review & editing. Deren Yang: supervision. Xuegong Yu: funding acquisition, project administration.

Conflicts of interest

There are no conflicts to declare.

Acknowledgements

Notes and references

1 E. R. Jones, M. F. P. Bierkens, P. J. T. M. van Puijenbroek, L. P. H. van Beek, N. Wanders, E. H. Sutanudjaja and M. T. H. van Vliet, *Nat. Water*, 2023, **1**, 602–613.

2 A. du Plessis, *One Earth*, 2022, **5**, 129–131.

3 G. M. Shayo, E. Elimbinzi, G. N. Shao and C. Fabian, *Bull. Natl. Res. Cent.*, 2023, **47**, 113.

4 M. Ismail, K. Akhtar, M. I. Khan, T. Kamal, M. A. Khan, M. A. A, J. Seo and S. B. Khan, *Curr. Pharm. Des.*, 2019, **25**, 3645–3663.

5 S. Khan, T. Noor, N. Iqbal and L. Yaqoob, *ACS Omega*, 2024, **9**, 21751–21767.

6 N. Liu, Z. Sun, H. Zhang, L. H. Klausen, R. Moonhee and S. Kang, *Sci. Total Environ.*, 2023, **875**, 162603.

7 J. Liu, N. Ma, W. Wu and Q. He, *Chem. Eng. J.*, 2020, **393**, 124719.

8 M. Fang, X. Tan, Z. Liu, B. Hu and X. Wang, *Research*, 2021, **2021**, 9794329.

9 W. Jiang, B. Q. L. Low, R. Long, J. Low, H. Loh, K. Y. Tang, C. H. T. Chai, H. Zhu, H. Zhu, Z. Li, X. J. Loh, Y. Xiong and E. Ye, *ACS Nano*, 2023, **17**, 4193–4229.

10 M. Liu, Q. Kang, Z. Xie, L. Lu, K. Dai and G. Dawson, *J. Phys. D: Appl. Phys.*, 2021, **55**, 043002.

11 I. S. Saputra, Y. Yulizar, R. P. Arindra, D. Annas, K. C. Sembiring and Sudirman, *Int. J. Environ. Res.*, 2023, **18**, 8.

12 I. Ahmad, Y. Zou, J. Yan, Y. Liu, S. Shukrullah, M. Y. Naz, H. Hussain, W. Q. Khan and N. R. Khalid, *Adv. Colloid Interface Sci.*, 2023, **311**, 102830.

13 X. Liu, J. Iocozzia, Y. Wang, X. Cui, Y. Chen, S. Zhao, Z. Li and Z. Lin, *Energy Environ. Sci.*, 2017, **10**, 402–434.

14 X. Jiang, J. Huang, Z. Bi, W. Ni, G. Gurzadyan, Y. Zhu and Z. Zhang, *Adv. Mater.*, 2022, **34**, e2109330.

15 J. Chen, Y. Chen, J. Shuai, X. Chen, D. Zhang, X. Lu, X. Fang, B. Zou, X. Yu, F. Zhao and W. Feng, *J. Alloys Compd.*, 2024, **1009**, 176938.

16 A. Guzmán-Cruz, M. Pal, F. Paraguay-Delgado, M. Vázquez-Lepe and U. Pal, *ChemistrySelect*, 2023, **8**, e202301198.

17 S. Mishra and B. Sundaram, *Mater. Today: Proc.*, 2024, **102**, 393–409.

18 A. Ayati, A. Ahmadpour, F. F. Bamoharram, B. Tanhaei, M. Manttari and M. Sillanpaa, *Chemosphere*, 2014, **107**, 163–174.

19 S. Lee, D. Kang, S. Jeong, H. Do and J. Kim, *ACS Omega*, 2020, **5**, 4233–4241.

20 N. González-Ballesteros, P. M. Martins, C. J. Tavares and S. Lanceros-Méndez, *J. Ind. Eng. Chem.*, 2025, **143**, 526–537.

21 M. Guan, J. Wang, K. Wang, J. Wang, R. Devasenathipathy, S. He, L. Yu, L. Zhang, H. Xie, Z. Li and G. Lu, *J. Colloid Interface Sci.*, 2023, **633**, 1033–1041.

22 S. Liu, W. Xu, Y. Niu, B. Zhang, L. Zheng, W. Liu, L. Li and J. Wang, *Nat. Commun.*, 2019, **10**, 5790.

23 A. Chrouda, S. Mahmoud Ali Ahmed and M. Babiker Elamin, *ChemBioEng Rev.*, 2022, **9**, 248–264.

24 D. Zhou, Y. Liu, W. Zhang, W. Liang and F. Yang, *Thin Solid Films*, 2017, **636**, 490–498.

25 H. Ichou, N. Arrousse, E. Berdimurodov and N. Aliev, *Journal of Bio- and Tribo-Corrosion*, 2023, **10**, 3.

26 Z. Ye, P. Lu, Y. Chen, Z. Xu, H. Huang, M. Zhi, Z. A. Chen and B. Yan, *Lab Chip*, 2024, **24**, 2253–2261.

27 Y. K. Abdel-Monem, S. M. Emam and H. M. Y. Okda, *J. Mater. Sci.: Mater. Electron.*, 2016, **28**, 2923–2934.

28 A. Barakat, M. Al-Noaimi, M. Suleiman, A. S. Aldwayyan, B. Hammouti, T. Ben Hadda, S. F. Haddad, A. Boshaala and I. Warad, *Int. J. Mol. Sci.*, 2013, **14**, 23941–23954.

29 D. C. Onwudiwe, N. H. Seheri, L. Hlungwani, H. Ferjani and R. Rikhotso-Mbungela, *J. Mol. Struct.*, 2024, **1317**, 139084.

30 D. Wostek-Wojciechowska, J. K. Jeszka, P. Uznański, C. Amiens, B. Chaudret and P. Lecante, *Mater. Sci.-Pol.*, 2004, **22**, 407–413.

31 Z. Abbasi, M. Salehi, A. Khaleghian and M. Kubicki, *Appl. Organomet. Chem.*, 2018, **32**, e4542.

32 K. Gangwar and P. Jeevanandam, *J. Mol. Struct.*, 2023, **1285**, 135423.

33 M. Goudarzi, H. A. Alshamsi, M. Amiri and M. Salavati-Niasari, *Arabian J. Chem.*, 2021, **14**, 103316.

34 P. Jubu, F. Yam, V. Igba and K. Beh, *J. Solid State Chem.*, 2020, **290**, 121576.

35 L. Liccardo, M. Bordin, P. Sheverdyaeva, M. Belli, P. Moras, A. Vomiero and E. Moretti, *Adv. Funct. Mater.*, 2023, **33**, 2212486.

36 T. Deka and R. G. Nair, *Int. J. Hydrogen Energy*, 2024, **59**, 322–342.

37 M. B. Kanoun, F. Ahmed, C. Awada, C. Jonin and P.-F. Brevet, *Int. J. Hydrogen Energy*, 2024, **51**, 907–913.

38 Z. Wu, P. Yang, Q. Li, W. Xiao, Z. Li, G. Xu, F. Liu, B. Jia, T. Ma, S. Feng and L. Wang, *Angew. Chem., Int. Ed.*, 2023, **62**, e202300406.

39 R. Jia, Y. Wang, C. Wang, Y. Ling, Y. Yu and B. Zhang, *ACS Catal.*, 2020, **10**, 3533–3540.

40 J. Wang, D. Tafen, J. Lewis, Z. Hong, A. Manivannan, M. Zhi, M. Li and N. Wu, *J. Am. Chem. Soc.*, 2009, **131**, 12290–12297.

41 M. Khan, S. Ansari, D. Pradhan, M. Ansari, D. Han, J. Lee and M. Cho, *J. Mater. Chem. A*, 2014, **2**, 637–644.

42 A. Borchers and T. Pieler, *Genes*, 2010, **1**, 413–426.

43 A. Farghaly, E. Maher, A. Gad and H. El-Bery, *Appl. Water Sci.*, 2024, **14**, 228.

44 Y. Yue, X. Yue, X. Tang, L. Han, J. Wang, S. Wang and C. Du, *Heliyon*, 2024, **10**, e30817.

45 M. Qi, Q. Lin, Z. Tang and Y. Xu, *Appl. Catal., B*, 2022, **307**, 121158.

46 A. Chaturvedi, P. Mondal, V. Srihari and M. Joshi, *Opt. Mater.*, 2023, **138**, 113732.

47 J.-P. Sylvestre, S. Poulin, A. V. Kabashin, E. Sacher, M. Meunier and J. H. T. Luong, *J. Phys. Chem. B*, 2004, **108**, 16864–16869.

48 Y. Zhang, J. X. Liu, K. Qian, A. Jia, D. Li, L. Shi, J. Hu, J. Zhu and W. Huang, *Angew Chem. Int. Ed. Engl.*, 2021, **60**, 12074–12081.

49 N. Kruse and S. Chenakin, *Appl. Catal., A*, 2011, **391**, 367–376.

50 M. A. Ibrahem, E. Verrelli, A. M. Adawi, J. G. Bouillard and M. O'Neill, *ACS Omega*, 2024, **9**, 10169–10176.

51 M. Sayed, J. Yu, G. Liu and M. Jaroniec, *Chem. Rev.*, 2022, **122**, 10484–10537.

52 A. Bondarev, S. Mihai, A. K. Usman, D. L. Cursaru, D. Matei, V. Sătulu, C. Gheorghe, G. Brănoiu and R. Șomoghi, *Nanomaterials*, 2024, **14**, 1780.

53 X. Yang, H. Fu, W. Wang, S. Xiong, D. Han, Z. Deng and X. An, *Appl. Surf. Sci.*, 2020, **505**, 144631.

54 S. Dong, G. T. Tebbutt, R. Millar, N. Grobert and B. M. Maciejewska, *Mater. Des.*, 2023, **234**, 112318.

55 H. Yu, S. Li, S. Peng, Z. Yu, F. Chen, X. Liu, J. Guo, B. Zhu, W. Huang and S. Zhang, *Int. J. Hydrogen Energy*, 2023, **48**, 975–990.

56 N. Ben Saber, A. Mezni, A. Alrooqi and T. Altalhi, *J. Mater. Res. Technol.*, 2021, **12**, 2238–2246.

57 J. Piedra-López, L. A. Calzada, P. Guerra-Blanco, J. Ortíz-Landeros, I. Elizalde-Martínez, M. A. Valenzuela and E. Albiter, *Catal. Today*, 2024, **432**, 114610.